Numerical phase change model considering crystal growth under supercooling

Huang, Haotian; Fan, Jianhua; Lin, Jianquan; Zhao, Qian; Zhang, Yuyue; Xiao, Yimin

Published in:
Applied Thermal Engineering

Link to article, DOI:
10.1016/j.applthermaleng.2021.117685

Publication date:
2022

Document Version
Peer reviewed version

Numerical phase change model considering crystal growth under supercooling

Haotian Huang[a,b], Jianhua Fan[b], Jianquan Lin[a], Qian Zhao[a], Yuyue Zhang[c], Yimin Xiao[a,*]

[a] *School of Civil Engineering, Chongqing University, Chongqing 400045, China*
[b] *Department of Civil Engineering, Technical University of Denmark, Brovej 118, 2800 Kgs. Lyngby, Denmark*
[c] *Department of Management, Technical University of Denmark, Brovej 118, 2800 Kgs. Lyngby, Denmark*

* Corresponding author. School of Civil Engineering, Chongqing University, Chongqing, 400045, China.
E-mail address: xiaoyimin@cqu.edu.cn (Y. Xiao)

Abstract: The supercooling of phase change material (PCM) significantly affects the heat release characteristics of heat storage systems. Therefore, accurate numerical modeling of the solidification process is key for studying heat storage. Few models considering the crystal growth of supercooling PCMs have been established; however, their accuracy under slight supercooling conditions is unsatisfactory. In this study, the implicit finite difference method was used to establish a two-dimensional PCM heat transfer model that considers the crystal growth process in detail. The growth rate of the crystallization front was used to control the crystallization start time at each node, and the solidification speed was used to manage the heating process once the crystallization was triggered. The accuracy of the model was verified by the experimental results obtained by melting, cooling, and triggering crystallization in a stable supercooled state and during cooling. Based on the simulations of a concentric tube PCM heat exchanger, the effects of several parameters on the heat release rate were investigated, such as the supercooling degree, the PCM initial temperature, and the inlet temperature of Heat transfer fluid (HTF). The results show that a large supercooling degree will accelerate the heat release rate of the PCM heat exchanger after the crystallization is triggered. An increase in the initial PCM temperature reduces the sharp increase in HTF outlet temperature caused by crystallization; a decrease in HTF inlet temperature also has the same effect. A comparison of various models demonstrated that the use of the crystallization front to calculate the PCM temperature directly causes up to 3% of the heat to be released earlier or later. Moreover, ignoring the crystal growth process causes up to 9% of the heat to be released in advance, and ignoring the supercooling causes an even greater error.

Keywords: crystal growth, phase change hysteresis, phase change material, solidification model, supercooling

Nomenclature

c	specific heat (J/(kg·K))
f	solidification degree (-)
g	crystallization fraction (-)
G	free energy (J/kg)
h	convection heat transfer coefficient (W/m^2·K)
H	enthalpy (J/kg)
L	latent heat (J/kg)
Nu	Nusselt number (-)

p pressure (Pa)

Pr Prandtl number (-)

q heat exchange (W/m^2)

Q energy (J)

$Qout$ output energy (J)

r radius (m)

Δr radial length of grid (m)

Re Reynolds number

$s(i)$ the length swept by the solidification front in cell i (m)

S entropy (J/kg·K)

$\dot{S}$ energy source item (W/m^3)

t time (s)

Δt time step (s)

T temperature (K)

ΔT degree of supercooling (^oC)

u axial velocity of heat transfer fluid (m/s)

U internal energy (J/kg)

v speed of crystallization front (m/s)

vs solidification speed (m/s)

V volume (m^3)

Δx axial length of grid (m)

$y(i)$ the length swept by the crystallization front in cell i (m)

σ specific surface energy (J/m^2)

ρ density (kg/m^3)

λ thermal conductivity (W/(m·K))

θ phase change interval (K)

Subscripts

col cooling

com complete model

H heat transfer fluid

i inner

in inlet

nuc crystal nucleus

k k^{th} iteration

l liquid

m phase change

o outer

out outlet

s solid

sup supercooling

w wall

Acronyms

DSC Differential scanning calorimetry

EG Expanded graphite

HTF Heat transfer fluid

PCM Phase change material

SAT Sodium acetate trihydrate

TMA Tridiagonal matrix algorithm

1. Introduction

The exacerbation of the energy crisis has promoted the development of renewable energy sources, such as solar and wind energy sources. As the application of renewable energy is affected by weather conditions, the primary problems are volatility and the mismatch of time and space. Thermal energy storage systems can regulate the supply and demand by storing and releasing heat, which can improve the energy utilization efficiency. Phase Change Materials (PCMs) are considered the most suitable storage media for the thermal management of renewable energy [1]. Compared to sensible heat storage, latent heat storage offers the advantages of high heat storage density (usually between 100 and 300 kJ/kg [2]) and a constant charge/discharge temperature. Moreover, it has a lower cost and is safer and more convenient than chemical heat storage.

The required temperature for building energy consumption is often lower than 100 °C, such as domestic hot water systems (55 to 65 °C) and heating systems (45 to 60 °C) [3]. PCMs that are suitable for use in this range generally include organic materials (e.g., paraffin, fatty acids, and alcohols) and inorganic materials (e.g.,

hydrated salts). In recent years, inorganic salts have attracted extensive attention owing to their very high latent heat, abundant resources, easy availability, low price, and environmental friendliness [4, 5]. Supercooling is one of the main problems encountered in the application of hydrated salts; when these materials are cooled to the phase transition temperature, they cannot be transformed from liquids to solids [6]. Crystallization is triggered when the temperature decreases to a specific value, which can be influenced by impurities or the actual working conditions, and then the temperature increases rapidly toward the phase transition temperature. In general, the degree of supercooling that is required for the crystallization of hydrated salts is high and inconsistent [5]. Studies have demonstrated that this value may even exceed 50 °C [7]. This results in a sudden, substantial release of latent heat at the beginning of solidification, as well as a reduction in the heat that is released in the subsequent discharge process [8].

Therefore, supercooling significantly affects the heat release curve of the heat storage unit. For this reason, it is essential to consider the supercooling state, crystallization growth, and temperature change during the solidification process in PCM phase change simulations. Several studies assumed that the PCM crystallization is instantaneous. Bony et al. improved the type 60 module in TRNSYS to incorporate PCMs [17]. Their model included the characteristics of hysteresis and supercooling but did not consider the crystallization growth process. With this model, once a node has solidified, the state of all points is calculated according to the cooling line. The authors carried out a supercooled solidification experiment in which a mixture of sodium acetate trihydrate (SAT) and expanded graphite (EG) was solidified in a cylindrical container, and the temperature changes at several points were monitored. Their results revealed a significant difference between the numerical and experimental results. Delcroix et al. constructed a one-dimensional heat transfer model to simulate the PCM walls [18]. During the temperature increase process at the crystallization cell, the temperature of the other cells was forcibly increased to the same value, while ensuring that their enthalpy value remained unchanged. Once crystallization of a cell was completed, the temperature of each cell was calculated according to the cooling line. However, the crystallization speed was related to the supercooling degree. Because a long time may be required to complete the overall crystallization under slight supercooling [19], ignoring the crystal growth will introduce errors.

The solid fraction is crucial to investigate the crystal growth process. Günther et al. expressed the solidification degree as a solid phase fraction, which takes the integer values 0 or 1 to indicate whether the material is entirely liquid or solid, respectively, and takes a number between 0 and 1 to indicate the mushy state during phase change [20]. The PCM temperature was calculated by a weighted averaging of the liquid and solid temperatures based on the solid fraction. The solid fraction was calculated from the crystal growth rate that was fitted to the experimental data. It was assumed that the solidification of one cell started only after the solid fraction of the adjacent cell reached 1. Zhou and Han noted that the process of supercooled solidification includes three stages: a stable supercooling period, a crystallization triggering period (dynamic solidification), and a regular solidification period [21]. In the second period, the temperature increases rapidly to near the melting point even though the solid fraction is only 0.33. Therefore, the correspondence between the solid fraction of 1 and the melting temperature decelerates the solidification process. To solve this problem, Uzan et al. determined the relationship between the latent heat release and temperature change through energy conservation equation [22]. They assumed that each cell was adiabatic during dynamic solidification and calculated the maximum solid fraction in this period. Once it was reached, the model entered the regular solidification period. The simulation was compared with an experiment on supercooled gallium solidification in a cylindrical container, and the experimental and simulation results were in good agreement. Ma et al. adopted a similar method to simulate the solidification of a sodium acetate solution [23]. The solid fraction on the equilibrium enthalpy line with the same enthalpy was calculated and considered as the maximum value achievable in the dynamic solidification stage. In this model, the crystal growth rate was the speed of the crystal front as measured by a high-speed camera in [24] and [25]. According to this model, the temperature of a point should reach its maximum value soon after

the crystal front has passed. However, Huang [26] experimentally showed that it still takes time to achieve the highest temperature after the front has passed; thus, the solidification process may be accelerated in this method. Furthermore, the dynamic solidification process will last for a long duration in the case of slight supercooling, during which the heat is inevitably transferred to the surroundings. In this situation, regarding the process as adiabatic will cause certain deviations.

The asymmetry of the melting and solidification processes is another important issue that needs to be considered. In the generic two-phase model, which is used extensively for modeling the phase change, PCMs are represented by two separate phases. Various models have been developed on this basis, and they all consider that phase transition occurs within a temperature range, rather than at a specific temperature. The difference between the models is the description of the transition process with the phase fraction [9]. In the static direct mapping model, one temperature corresponds to one phase fraction, so that a liquid ratio leads to the same temperature regardless of the melting or solidification process. In fact, using the differential scanning calorimetry (DSC) step measurement method, Jin et al. proved that the melting and solidification processes of PCMs are asymmetric [10]. In a subsequent study, they constructed a one-dimensional heat transfer model with asymmetric energy and experimentally showed that the energy asymmetric model was more accurate than the symmetric model [11]. This difference in the temperature range of the phase transition is known as phase change hysteresis. Tabares-Velasco et al. used only one corresponding relationship between the enthalpy and temperature and argued that the model would be inaccurate under strong hysteresis [12]. Biswas et al. studied the phase transition hysteresis using a PCM wall model and argued that the hysteresis had a significant impact on the thermal performance of the PCM layer resulting in a considerable reduction in the energy saving [13].

The static hysteresis model, which is based on the static direct mapping model, incorporates a term to characterize the heating or cooling process [14]. Goia et al. developed an algorithm that considered hysteresis in EnergyPlus™, and they set two enthalpy–temperature curves for melting and solidification, respectively [15]. A comparison with the experimental results demonstrated that the model was more accurate than previous models. The melting and solidification kinetic model is based on the reversible reaction between the phases. When the conversion rates of the two phases are equal, the phase transfer reaches a steady state. In the solidification kinetic model, the melting process is calculated using the static model, and the nucleation probability per unit time is calculated using the PCM and equilibrium temperatures for the solidification process [16].

In this study, a two-dimensional phase-change heat transfer numerical model was constructed. The model considers the asymmetry of the melting and solidification, supercooling characteristics, and crystal growth process after crystallization is triggered. Moreover, the relationships among the solid fraction, crystal growth rate, and temperature change were optimized. Using a SAT and EG composite material, an experimental system of the PCM concentric tube exchanger was constructed. The accuracy of the numerical model was verified via the experimental data of the melting and cooling cases, the triggering of crystallization in the stable supercooling case, and the triggering of crystallization in the cooling process case. The influence of the input parameters, namely the supercooling degree, inlet temperature, and initial temperature, on the heat exchanger performance was studied. Furthermore, the model developed in this study was compared to a model that neglects supercooling, a model that neglects crystal growth, and a model that correlated the temperature only with the crystal growth.

2. Numerical model

2.1 Model description

The enthalpy method and effective heat capacity method are generally employed to deal with the phase-change process [27]. In the enthalpy method, the enthalpy–temperature curve is used to calculate the temperature

through enthalpy [28]. In the effective heat capacity method, the latent heat is evenly distributed in the phase-change interval and added to the specific heat capacity. Subsequently, the phase-change problem is transformed into a nonlinear heat conduction problem. Our model is based on the enthalpy method. Fig. 1 shows the relationship between the enthalpy and temperature of the PCM. In an ideal situation, the phase change is completed at a specific temperature, which is called the phase change temperature T_m. However, the actual phase change occurs within a temperature interval. Under heating conditions, the enthalpy change follows A–B–C–D path, and the phase change occurs between B and C. As the phase transition hysteresis is considered, the phase change intervals of cooling and heating are different. Under cooling conditions, the enthalpy develops along D–E–N–A when no supercooling occurs.

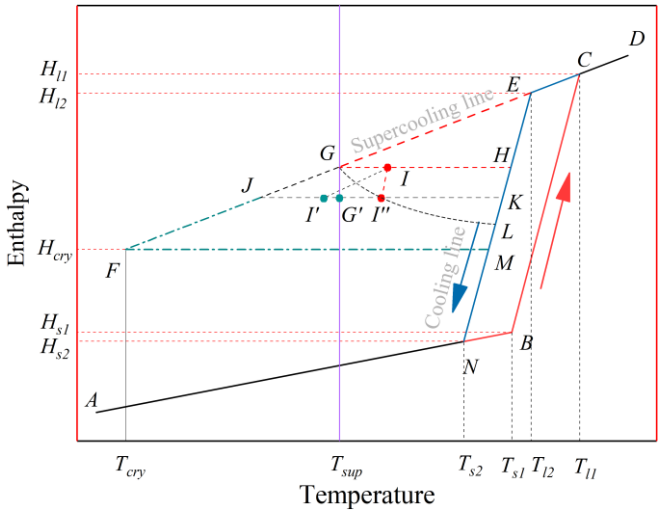

Fig. 1. Relationship between enthalpy and temperature

Next, the supercooling characteristic is considered. The free energy (G) of a material varies in different phases. Eq. (1) indicates that the free energy is inversely proportional to the entropy under a constant pressure. The molecules in the liquid phase are more "disordered," and thus have higher entropy than those in the solid phase. Owing to the different change rates of free energy, the G–T lines of the two phases intersect at one point, which corresponds to the phase-change temperature, as illustrated in Fig. 2.

$$G = H - TS, \tag{1}$$

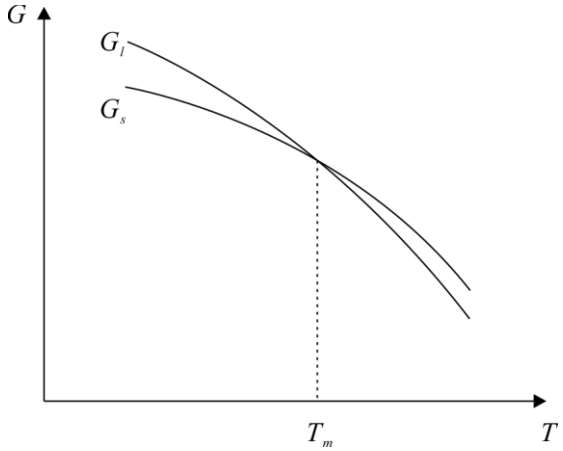

Fig. 2. Free energy–temperature curves of liquid and solid states

When the material is transformed from the liquid to solid phase, the energy change ΔG_B can be calculated as follows:

$$\Delta G_B = (H_l - H_s) - T(S_l - S_s), \tag{2}$$

The phase transition indicates the appearance of solid particles (crystal nuclei). As the atoms on the surface

of a crystal nucleus appear in a force-asymmetric position, their free energy needs to be increased. The inner atoms are in a state of force symmetry and their free energy decreases. The total change in the free energy ΔG of all atoms is the energy required for the phase transition [29] and it can be expressed as follows [30]:

$$\Delta G = -\frac{4}{3}\pi {r_{nuc}}^3 \rho \Delta G_B + 4\pi {r_{nuc}}^2 \sigma, \tag{3}$$

When T is equal to the phase change temperature T_m, the free energy change is 0, which means that crystallization cannot occur. In this case, the following equation can be derived:

$$S_l - S_s = \frac{H_l - H_s}{T_m} = \frac{L}{T_m}, \tag{4}$$

Because $S_l - S_s$ can be considered as a constant when $T < T_m$, Eq. (2) can be rewritten as

$$\Delta G_B = L\left(1 - \frac{T}{T_m}\right) = \frac{L}{T_m}\Delta T, \tag{5}$$

Thus, the change in the free energy increases linearly with the supercooling degree; i.e., the supercooling provides the required power for the phase transformation. Therefore, in Fig. 1, when the material is cooled to the phase transition region (point E), it does not solidify directly along E–N, but it continues to release heat in the form of sensible heat along the D–E direction until point F, when the supercooling can provide sufficient power for solidification. This phenomenon of crystallization is known as homogeneous nucleation. Once a crystal appears, the specific surface area of the surrounding nucleus changes, and the energy required for crystallization is reduced. Overall, the crystal grows around, which is known as heterogeneous nucleation. Therefore, the injection of nuclei into supercooled material can also trigger the solidification process.

This process must be numericalized before describing the solidification process. The implicit finite difference method was used to construct the numerical model. The computational domain was divided into several cells for the one-dimensional model. The energy and momentum equations were calculated for each cell to represent their states. As illustrated in Fig. 3, the crystallization front grows forward at the crystallization speed v; the crystallization fraction $g(i)$ is used to represent the proportion of the area that is swept by the front in each cell. When $g(i)$ reaches 1, the next cell starts to solidify. Some studies have only used $g(i)$ as the solid fraction to calculate the temperature [20] [22] [23], which causes deviations. In this study, the solidification speed vs is introduced to indicate the solidification degree $f(i)$ when each cell starts to solidify.

$$g(i) = \frac{\mathrm{y}(i)}{\Delta x} = \begin{cases} \frac{\int_{t0(i)}^{t} v(i)dt}{\Delta x}, & y(i) < \Delta x, \\ 1, & y(i) \geq \Delta x, \end{cases} \tag{6}$$

$$f(i) = \frac{\mathrm{s}(i)}{\Delta x} = \begin{cases} \frac{\int_{t0(i)}^{t} vs(i)dt}{\Delta x}, & s(i) < \Delta x, \\ 1, & s(i) \geq \Delta x, \end{cases} \tag{7}$$

where $t0(i)$ is the time when cell i starts to solidify. Crystallization fraction $g(i)$ and solidification degree $f(i)$ with values of 0 imply that the cell has not yet started to solidify, whereas $g(i) = 1$ means that the cell has solidified completely. Moreover, vs is used to calculate the time required for the solidification of each cell to be completed. The crystallization speed v and solidification speed vs of the SAT/EG composite material can be calculated as follows [26]:

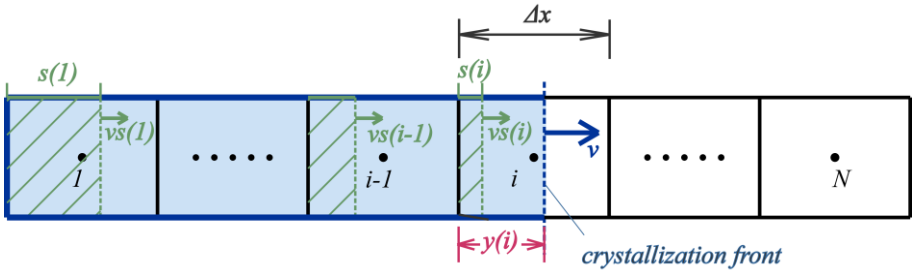

Fig. 3. Representation of solidification process in one-dimensional model

$$v = 4.15(1 - e^{-0.44\Delta T})^{22.96}, \tag{8}$$

$$vs = \frac{\Delta x}{19.34+\exp\left(-32+0.718(T-273.15)\right)}. \tag{9}$$

In Fig. 1, the temperature of the isenthalpic projection point (G) on the supercooling line (EF) of any point (I) in the solidification process is denoted as T_{sup}, and the temperature of the isenthalpic projection point (H) on the cooling line (EN) is denoted as T_{col}. The temperature of point I can be calculated using Eq. (10).

Assuming that the material starts to solidify from point G, the state will change to point I along G–H under adiabatic conditions in the next time step. The position of point I can be calculated using Eq. (11). However, with the increase in the temperature, heat is transferred to the adjacent cells, resulting in a decrease in enthalpy to the J–K line. Under the same solidification degree, the real state point should be I' instead of I (GI / GH = JI' / JK). It is unreasonable for the temperature of the heat source to be lower than that of the surrounding points (T(I') < T (G')). To avoid this error, the model retains the temperature of the projection point at the last time step (T (G')) if the enthalpy decreases in the crystallization process of a cell. Therefore, Eq. (11) is modified to Eq. (12); thus, the state point at the new time step should be I'' (G'I'' / G'K = GI / GH). The actual curve of the solidification process should be G–I''–L. Once the crystallization is completed, the PCM remains in the phase-change zone, releasing heat in the form of latent heat and cooling along L–N to point N, and subsequently releasing sensible heat along N–A.

$$T(i) = \begin{cases} \mathrm{T}_{sup}, & \mathrm{f(i)} = 0 \\ \mathrm{T}_{sup} + \mathrm{f(i)} \cdot (\mathrm{T}_{col} - \mathrm{T}_{sup}), & 0 < \mathrm{f(i)} < 1 \\ \mathrm{T}_{col}, & \mathrm{f(i)} = 1 \end{cases} \tag{10}$$

$$GI = \mathrm{f(i)} \cdot \mathrm{GH} \tag{11}$$

$$G'I'' = \mathrm{f(i)} \cdot \mathrm{G'K} \tag{12}$$

2.2 Model construction

The numerical model used in this study was established in a cylindrical coordinate system. The cell division depicted in Fig. 3 was expanded into that shown in Fig. 4. There are two situations that cause a cell to crystallize: the temperature is lower than the crystallization temperature or the cell is in a supercooled state and at least one adjacent cell has finished crystallization. Therefore, after a crystal appears, it will grow to the surrounding cells. Cellular automata [31] were used to define the direction of the crystallization growth. When a cell is completely swept by the crystallization front, it becomes a source, and the adjacent cells begin to crystallize. The moving direction and moving distance of the crystallization front in these cells are dependent on their relative position to the source cell. For example, when cell 1 is completely swept (Fig. 4a), the adjacent cells 2, 4, and 5 will begin to crystallize simultaneously; their crystallization front moves along the x-, r-, and diagonal-direction, respectively (as indicated in Fig. 4b), and their moving distances are Δx, Δr, and diagonal length Δl, respectively. Fig. 4c depicts a possible state after a certain period. The solidification of cells 3 and 6 is triggered simultaneously by cell 2, whereas the solidification of cells 7 and 8 is triggered by cell 4. Similar to the case in the one-

dimensional model, when each cell starts to solidify in the two-dimensional model, its solidification degree begins to deepen at the solidification speed calculated in Eq. (9). This is illustrated in Fig. 5.

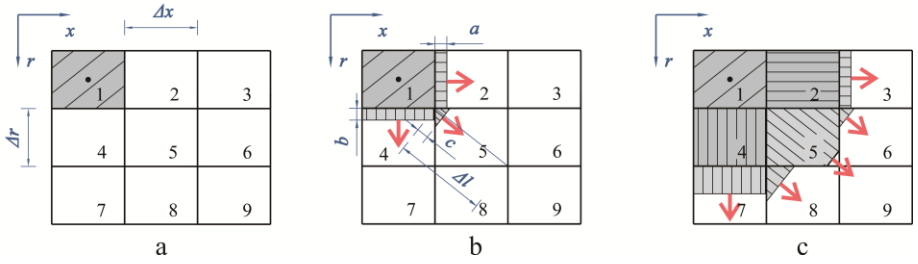

Fig. 4. Crystal growth direction of two-dimensional model

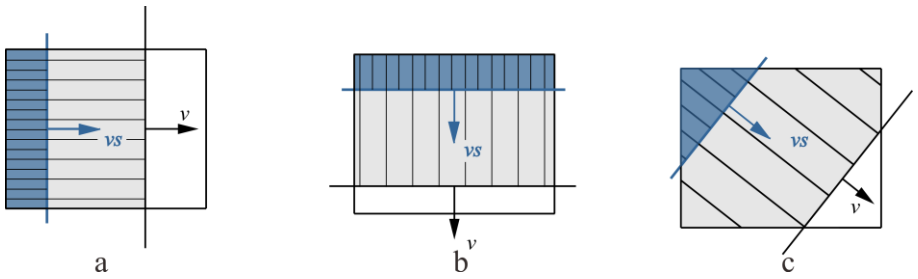

Fig. 5. Schematic of cell solidification

The following assumptions are made for the development of this model:

- The material is isotropic and uniformly filled.
- The outer surface of the heat exchanger is insulated.
- The convection in the PCM calculation domain is ignored because the PCM used in this study is shaped by the EG.
- The heat transfer fluid (HTF) exhibits no temperature difference in the radial direction.

For the PCM domain:

$$\rho\frac{\partial H}{\partial t}=\frac{1}{r}\frac{\partial}{\partial r}\left(\lambda r\frac{\partial T}{\partial r}\right)+\frac{\partial}{\partial x}\left(\lambda\frac{\partial T}{\partial x}\right)+\dot{S}, \tag{13}$$

The left side of the equation represents the increase in PCM enthalpy. The first and second terms on the right represent the heat conduction in the radial and axial directions, respectively. The last term is a source term, which represents the heat generated by the internal heat source per unit volume of PCM. In this model, the source term only plays a role at the junction of PCM and HTF, as shown in Eqs. 20– 22.

The corresponding relationship between the enthalpy and temperature of the heating process is expressed as follows:

$$H=\begin{cases}\int_0^T c_s\,dT, & T<T_{s1},\\ \int_0^{T_{s1}} c_s\,dT+\int_{T_{s1}}^{T}\frac{c_s+c_l}{2}dT+\frac{T-T_{s1}}{T_{l1}-T_{s1}}\cdot L_1, & T_{s1}\le T<T_{l1},\\ \int_0^{T_{s1}} c_s\,dT+\int_{T_{s1}}^{T_{l1}}\frac{c_s+c_l}{2}dT+L_1+\int_{T_{l1}}^{T} c_l\,dT, & T\ge T_{l1},\end{cases} \tag{14}$$

where T_{s1} and T_{l1} are the lower and upper bounds of the phase-change interval during the melting process, respectively, and L_1 is the latent heat for the melting process. For the solidification process without supercooling, T_{s1}, T_{l1}, and L_1 should be replaced by T_{s2}, T_{l2}, and L_2.

Owing to the phase-change hysteresis, the melting and solidification processes have different phase-change intervals, which are denoted as $T_{s1}-T_{l1}$ and $T_{s2}-T_{l2}$, respectively, in Fig. 1. To ensure the energy conservation of the two processes, the relationship between the latent heat and phase-change interval is determined as follows:

$$L_2 - L_1 = c_s(T_{s1} - T_{s2}) - c_l(T_{l1} - T_{l2}) + \frac{c_s+c_l}{2}((T_{l1} - T_{s1}) - (T_{l2} - T_{s2})), \quad (15)$$

When both phase-change intervals are θ, Eq. (15) can be written as

$$L_2 - L_1 = (c_s - c_l)\theta. \quad (16)$$

When supercooling is considered, based on Eqs. (14) and (10), the relationship between the enthalpy and temperature in the cooling process is expressed as follows:

$$T = \begin{cases} \frac{1}{c_s}H, & H < H_{s2}, \\ (H + \frac{c_l-c_s}{2}T_{s2} + \frac{T_{s2}}{T_{l2}-T_{s2}} \cdot L_2)/(\frac{c_s+c_l}{2} + \frac{L_2}{T_{l2}-T_{s2}}), & H_{s2} \le H < H_{cry}, \\ \mathrm{T}_{sup} + \mathrm{f(i)} \cdot (\mathrm{T}_{col} - \mathrm{T}_{sup}), & H_{cry} \le H < H_{l2}, \\ (H + \frac{c_l-c_s}{2}(T_{s2} + T_{l2}) - L_2)/c_l, & H \ge H_{l2}, \end{cases} \quad (17)$$

where T_{sup} and T_{col} can be calculated using Eqs. (18) and (19), respectively. It should be noted that T_{sup} may use the data of the previous time step, as described in section 2.1.

$$T_{sup} = (H + \frac{c_l-c_s}{2}T_{s2} + \frac{T_{s2}}{T_{l2}-T_{s2}} \cdot L_2)/(\frac{c_s+c_l}{2} + \frac{L_2}{T_{l2}-T_{s2}}) \quad (18)$$

$$T_{col} = (H + \frac{c_l-c_s}{2}(T_{s2} + T_{l2}) - L_2)/c_l \quad (19)$$

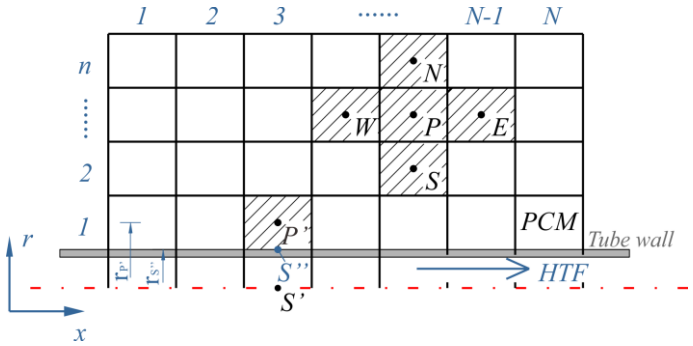

Fig. 6. Schematic of numerical model

An additional heat source method is used to handle the heat transfer between the PCM and HTF. Using the inner node P' in Fig. 6 as an example, a virtual node S'' is created on the boundary, and the heat exchange can be obtained using Eq. (20). Subsequently, the term S'' can be eliminated using Eq. (21), and the source term in Eq. (13) can be expressed by Eq. (22).

$$\mathrm{q} = h(T_{S'} - T_{S''}) = \frac{T_{S''}-T_{P'}}{\Delta r/2\lambda_s}, \quad (20)$$

$$\mathrm{q} = \frac{T_{S'}-T_{P'}}{\frac{1}{h}+\frac{\Delta r}{2\lambda_{S'}}}, \quad (21)$$

$$\dot{S} = \frac{T_{S'}-T_{P'}}{\frac{1}{h}+\frac{\Delta r}{2\lambda_{S'}}} \cdot \frac{r_{S''}}{r_{P'} \cdot \Delta r}, \quad (22)$$

where $\lambda_{s'}$ is the average thermal conductivity of nodes P' and S', h is the convection heat transfer coefficient, which can be calculated using Eq. (23), $r_{P'}$ is the radius of the node P' position, and $r_{S''}$ is the radius of the node S'' position, which is also the radius of the outer wall of the inner tube.

$$Nu=\begin{cases}3.66,\ 0<Re<2300\\ 0.012\left(Re_f{}^{0.87}-280\right)Pr_f{}^{0.4}\left[1+\left(\frac{d}{l}\right)^{\frac{2}{3}}\right]\left(\frac{Pr_f}{Pr_w}\right)^{0.11},\ 2300\le Re<1\times10^4\\ 0.023Re_f{}^{0.8}Pr_f{}^{0.4},\ Re\ge1\times10^4, T_w>T_H\\ 0.023Re_f{}^{0.8}Pr_f{}^{0.3},\ Re\ge1\times10^4, T_w<T_H\end{cases} \tag{23}$$

For the HTF,

$$\frac{\partial T}{\partial \tau}+u\frac{\partial T}{\partial x}=-\frac{2}{\rho_H\cdot c_H\cdot r}q, \tag{24}$$

where r is the radius of the inner tube. When the influence of the tube wall thickness is considered, r should be replaced by r_i^2/r_o, where r_i and r_o are the inner and outer radii of the inner tube, respectively.

2.3 Model solution

Using node P in Fig. 6 as an example, Eq. (13) can be discretized into Eq. (25) in the form of an implicit difference. It can be observed that its enthalpy and temperature are related to the temperature of nodes N, W, E, and S, as well as the enthalpy of node P at the previous time step. The temperature terms need to be converted into enthalpy terms to solve Eq. (25). Therefore, the relationship between these nodes is expressed by Eq. (26).

$$\frac{\rho\Delta r\Delta x r_p}{\Delta t}\left(H_P-H_P{}^0\right)=\frac{\lambda_N r_N\Delta x}{\Delta r}T_N+\frac{\lambda_S r_S\Delta x}{\Delta r}T_S+\frac{\lambda_E r_P\Delta r}{\Delta x}T_E+\frac{\lambda_W r_P\Delta r}{\Delta x}T_W-\left(\frac{\lambda_N r_N\Delta x}{\Delta r}+\frac{\lambda_S r_S\Delta x}{\Delta r}+\frac{\lambda_E r_P\Delta r}{\Delta x}+\frac{\lambda_W r_P\Delta r}{\Delta x}\right)T_P+\dot{S}, \tag{25}$$

$$H_P=F(H_P{}^0,T(H_N),T(H_S),T(H_E),T(H_W)), \tag{26}$$

where *T(H)* represents the relational expression for converting the enthalpy into the temperature according to Eq. (14) or (17), and *F(x)* denotes the expression of Eq. (25).

In this case, it is necessary to solve the five-diagonal matrix, which is complex and time consuming. Thus, we used the alternating direction implicit method, which performs the implicit calculation in the radial dimension and explicit calculation in the axial dimension. One radial scan and one axial scan are regarded as one iteration, and the calculation is repeated until the convergence standard is reached. In this method, Eq. (26) is adapted to Eq. (27). An equation group is formed by the energy equation of each node on a radial column and the energy equation of HTF in Eq. (24). Thereafter, the enthalpy value of each node and the temperature of the HTF node can be obtained using the tridiagonal matrix algorithm (TMA).

$$H_P=F(H_P{}^0,T(H_N),T(H_S),T\left(H_E{}^0\right),T\left(H_W{}^0\right)) \tag{27}$$

The calculation converges when the difference between the energy input (Q_{in}) and the energy change in the calculation domain (ΔQ) in each time step is less than the residual value according to Eqs. (28) to (30), and the enthalpy changes of all nodes in two adjacent iterations are less than the residual value according to Eq. (31).

$$|\mathrm{Qin}-\Delta\mathrm{Q}|<10^{-6}, \tag{28}$$

$$\mathrm{Qin}=(\mathrm{Tin}-\mathrm{Tout})\mathrm{c}_H\mathrm{m}_H\Delta t, \tag{29}$$

$$\Delta\mathrm{Q}=2\pi\rho_{PC}\Delta\mathrm{r}\Delta\mathrm{x}\sum_{i=1}^{N}\sum_{j=1}^{n}r(i,j)[H(i,j)-H(i,j)^0]+\pi r_{in}{}^2\Delta\mathrm{x}\mathrm{c}_H\rho_H\sum_{i=1}^{N}[T_H(i)-T_H(i)^0], \tag{30}$$

$$\max\left[H(i,j)^k-H(i,j)^{k-1}\right]<10^{-6}, \tag{31}$$

where the superscript 0 represents the value of the previous time step and the superscript k represents the value of the k^{th} iteration. The operation logic of the program is described in detail in Appendix 1.

To ensure that the simulation results are independent of the grid size, the simulations with grid numbers 10×5, 25×10, 50×10, 50×20, and 100×40 are compared. Fig. 7 shows the outlet temperature of HTF under the same boundary conditions. It can be seen that the grid number of 50×20 is enough to obtain accurate results,

since its result is almost the same as the result of 100×40. Therefore, the grid number of 50×20 is employed in the following investigation. To select a suitable time step, Fig. 8 compares the simulation results with time steps of 1s, 2s, 5 s, 10 s, 30 s, and 60 s. Because the results of the 1 s, 2 s, and 5 s cases are almost the same, 5 s is selected as the time step in the following investigation.

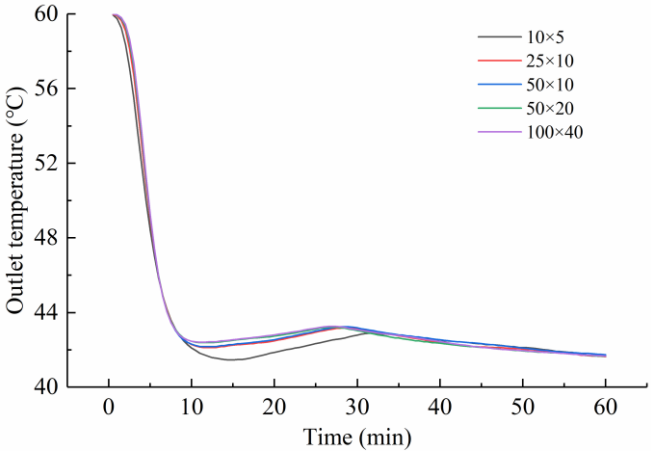

Fig. 7. Independence test of the grid size

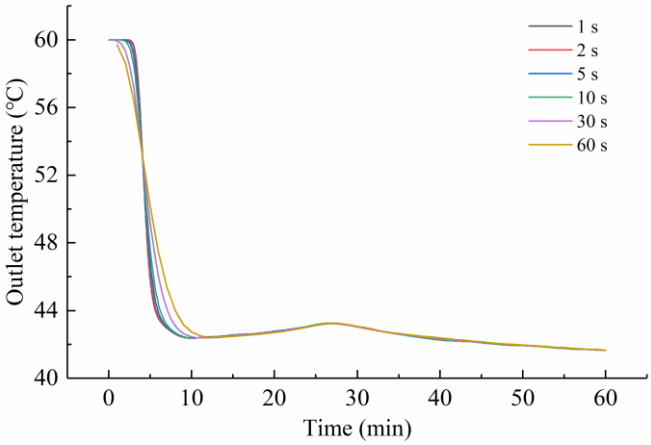

Fig. 8. Independence test of the time step

3. Model validation

3.1 Material preparation

SAT is an inorganic hydrated material used extensively for heat storage. It is often used for comparative research owing to its large and stable degree of supercooling [32]. In this study, a composite material consisting of 90 wt% SAT and 10 wt% EG was used as the PCM. The sample was first heated to 80 °C in a water bath for 2 h to ensure that they were completely melted and then placed in an 80 °C vacuum chamber for 24 h for the SAT to be fully absorbed by the EG. During this period, the samples were stirred several times to ensure uniformity. Subsequently, the thermal parameters of the sample were tested.

The cooling curve method was used to test the degree of supercooling of Sample 2. The latent heat and specific heat were measured using DSC (NETZSCH 200 F3). In the test, the PCM was heated from 20 to 90 °C at a rate of 5 °C/min, maintained for 10 min, and subsequently cooled at the same rate. The thermal conductivity was measured with a Hot Disk TPS 2500 CH using the transient plane source method. Temperatures of 40 and 70 °C were used to represent the solid and liquid states, respectively. The relevant thermal parameters are listed in Table 1.

Table 1
Properties of the phase change material (PCM) used in this study

Material	Phase change temperature (°C)	Specific heat (kJ/kgK)		Heat of fusion (kJ/kg)	Thermal conductivity (W/mK)	
		Solid	Liquid		Solid	Liquid
90% SAT +10% EG	57.5	1.92	3.43	239.6	2.33	2.29

3.2 Experimental facility and validation

Figures. 9 and 10 show the photograph and schematic of the experimental system constructed to verify the numerical model in this study, respectively. As shown in Fig. 10, the system consisted of a mold temperature machine to provide water at a stable temperature, a 40 L buffer tank, a flowmeter, and an experimental facility. An Agilent 3972A data acquisition instrument and laptop were used to record the data. The experimental facility was 1 m long and included two concentric tubes, as illustrated in Fig. 11. The inner tube was made of copper (inner diameter: 20.32 mm; outer diameter: 22 mm), and the outer tube was made of stainless steel (inner diameter: 61.12 mm; outer diameter: 63 mm). The space between the two tubes was filled with PCM (density: 914.5 kg/m^3) and the outer wall of the tube was well insulated. Water flowed through the inner tube at a specified temperature to exchange heat with the PCM. One end of the facility was equipped with semiconductor refrigeration chips, which could rapidly achieve local low temperatures and trigger PCM crystallization. Their hot surfaces were bonded with cooling plates using thermal conductive glue to ensure heat dissipation. Five calibrated K-type thermocouples (accuracy: ±0.2 °C) were set to record the inlet temperature, outlet temperature, and temperature change inside the PCM every 30 s. The location information is depicted in Fig. 11.

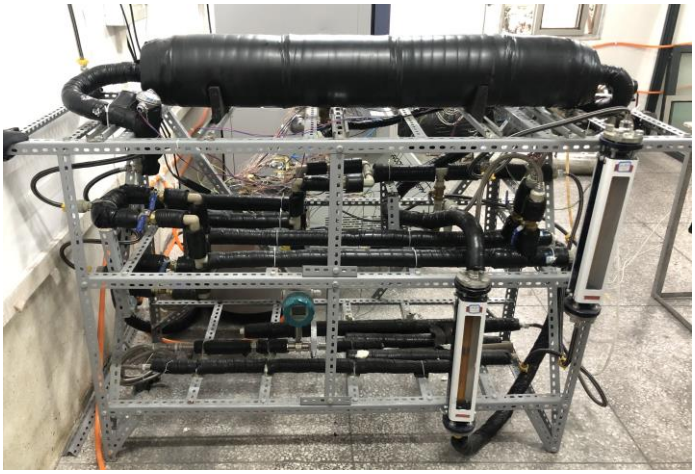

Fig. 9. Photograph of experimental system

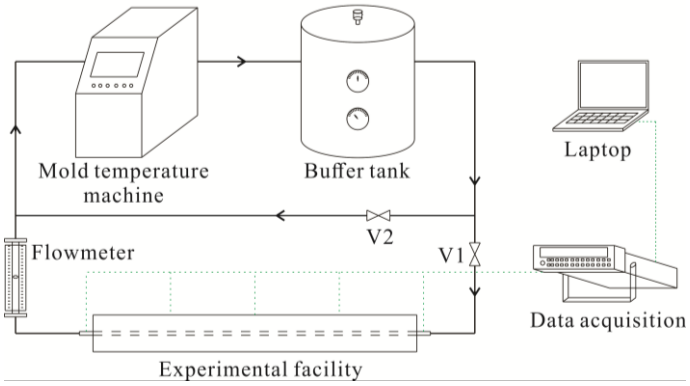

Fig. 10. Schematic of experimental system

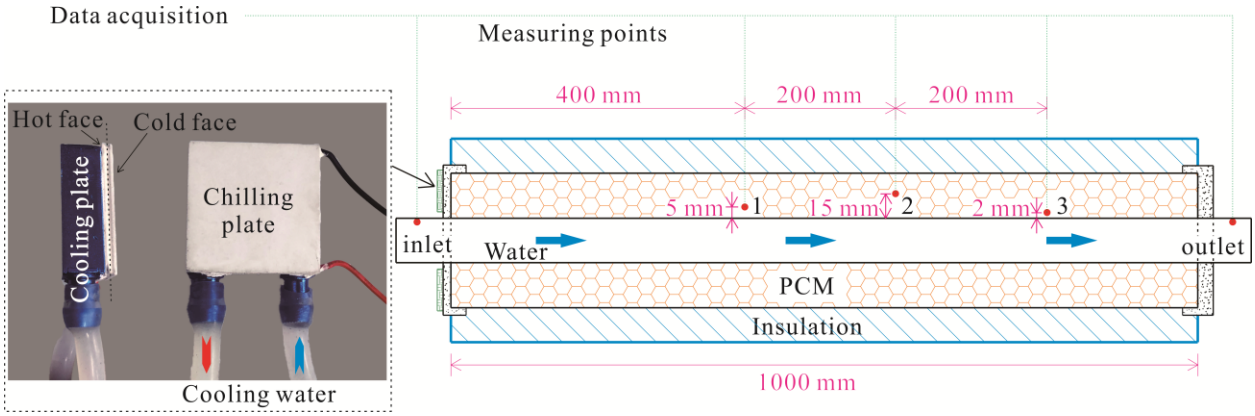

Fig. 11. Schematic of experimental facility

Three experiments were conducted by melting, cooling, and solidifying under stable supercooling. For the melting, the facility was connected to water at 19.4 °C for a sufficiently long time to ensure internal PCM temperature uniformity. Thereafter, valve 2 was turned on, valve 1 was turned off, and the water temperature was set to 83.2 °C. When the buffer tank temperature was the same as the set value, valve 1 was reopened and the flow rate was adjusted to 140 L/h. The numerical model adopted the same structural and physical parameters as those used in the experiment. Fig. 12 shows the temperature variations in the measuring points of the numerical simulation and experiment. It can be seen that the temperature changes were relatively similar at different points, with a slight deviation of point 2 before and after the phase transition process (approximately 10 and 33 min, respectively). The error could have arisen from the simplification of the heat capacity: the sudden shift in the specific heat capacity around the phase change temperature resulted in an abrupt change in the temperature change rate.

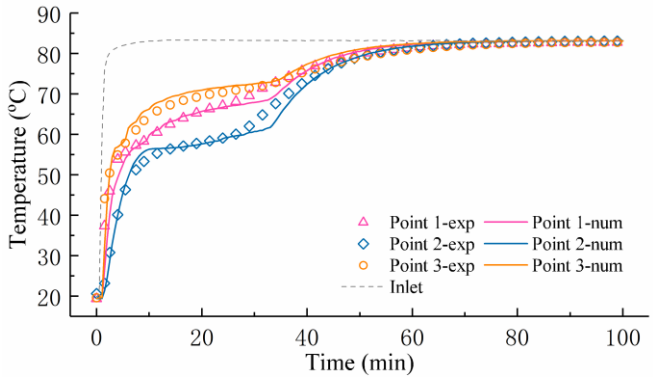

Fig. 12. Temperature variation at different points during melting

For the cooling case, the PCM was first heated to 82.5 °C and then cooled to 50.8 °C. The PCM did not

solidify owing to the supercooling characteristics. The same numerical model was verified under this case. As illustrated in Fig. 13, the simulation results were in good agreement with the experimental data, which demonstrates that the treatment of the supercooling process in this numerical model was accurate.

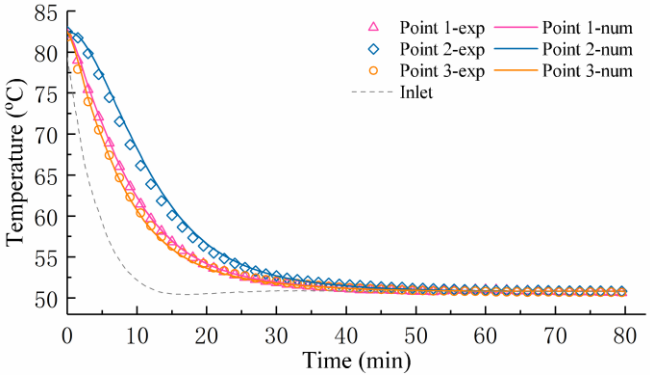

Fig. 13. Temperature variation at different points during cooling without supercooling

To demonstrate the temperature change of the solidification process more clearly and to verify the numerical model more convincingly, a slight supercooling state was selected for the solidification case. The PCM was first heated to 80 °C; then, water at 53.6 °C flowed through the experimental facility at a flow rate of 140 L/h for a sufficiently long time to ensure temperature uniformity of the PCM. Thereafter, the degree of supercooling was approximately 3.9 °C. The chilling plate was turned on for 30 s to achieve a short local low temperature. In this manner, the crystallization of the supercooled PCM was triggered, and the solidification process was started. As the operation of the chilling plate was transient and very quick compared to the characteristic time of the process, the effect of this operation was ignored in the numerical model. Fig. 14 shows the evolution of the numerical and experimental temperature at the measuring points during solidification. The simulation results demonstrate that the start time and temperature growth rate of the crystallization process at each point were in good agreement with the experimental data. This proves that the numerical model accurately reflected the crystal growth and solidification development. The temperature change at point 2 exhibited some deviations between 222 and 372 min. This is because the model simplified the deepening solidification at a uniform rate until it reached the highest temperature. However, the temperature increase reduced around the phase change temperature, which resulted in different trends. The outlet temperature comparison between the numerical results and the experimental results is shown in Fig. 15, in which the maximum deviation between the complete model and the experiment is 0.08 °C. Fig. 16 depicts the heat transfer rate between the PCM and HTF, and the total output energy in the solidification process. The total output energy of each case at different times was calculated using Eq. (32). It can be seen that the numerical results were consistent with the experimental data. For the case in which the PCM was triggered to crystallize during the cooling process, the experimental data in a literature were used to verify the model, and this work was demonstrated in our previous study [26]. The good agreement between the experimental and numerical results proved the accuracy of the model, which is referred to as the complete model in the rest of this paper. Moreover, Figs. 14, 15 and 16 show a comparison of the temperature and heat transfer evolution obtained with the complete model, single growth model, and experiments. In single growth model, the solidification speed was not considered, and the temperature was calculated directly based on the crystallization speed. Although the times for the triggering of crystallization at each point of the single growth and complete models were the same as those in the experiment, the single growth model significantly overestimated the temperature growth rate, causing notable errors.

$$Q_{out}(t) = \sum_{o=1}^{t/\Delta t}[(Tout(o) - Tin(o))c_H m_H \Delta t], \quad (32)$$

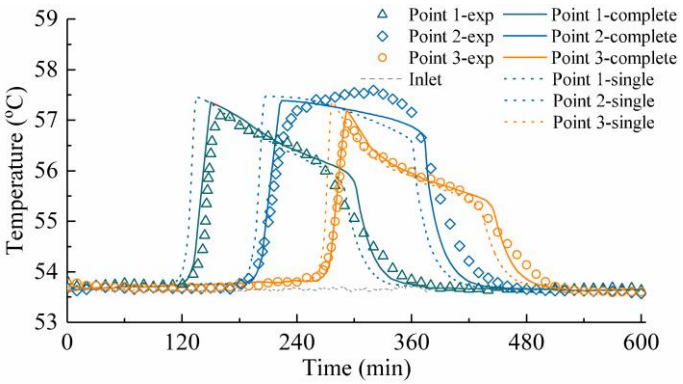

Fig. 14. Temperature variation during solidification

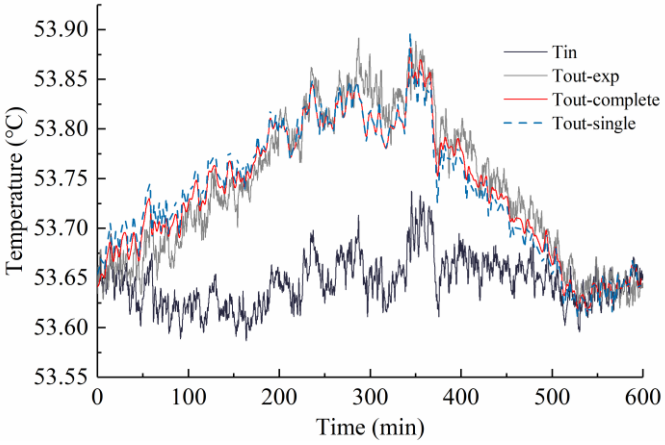

Fig. 15. Outlet temperature variation during solidification

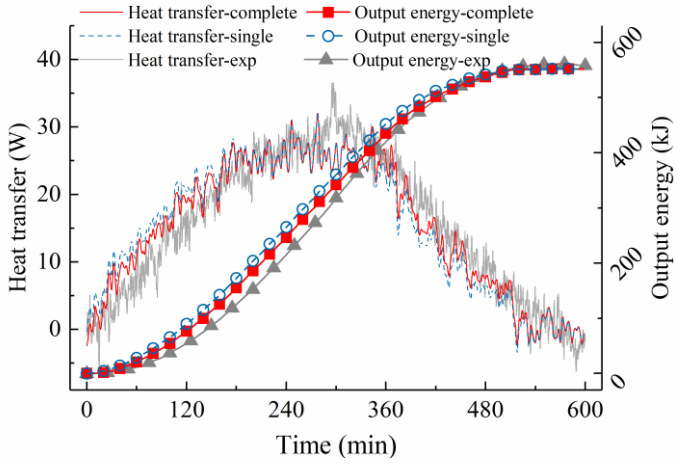

Fig. 16. Heat transfer during solidification

4. Results and discussion

4.1 Effect of supercooling on heat output

Figure. 17 compares the effects of different supercooling degrees on the outlet temperature and output power when the initial temperature was 60 °C and the inlet temperature was 40 °C, Since the output power has a linear relationship with the outlet temperature, they can be represented by the same curves and two ordinate axes. In all subsequent simulations, the inner diameter of the outer tube was 102 mm, the inner diameter and thickness of the inner tube were 30 mm and 1.5 mm, respectively, and the length was 1 m. The water flow rate

in the inner pipe was 10 L/h and the material parameters described in section 3.2 were used. There are 11 cases compared, and their supercooling degrees are assumed to be from 2 °C to 12 °C. It can be observed that after the crystallization was triggered, the outlet temperature increased significantly, and the maximum temperature increased with deepening supercooling. This is because a part of the heat was removed by the HTF during the PCM crystallization process, resulting in a decrease in the enthalpy. Serious supercooling can make this process faster and more adiabatic. In serious supercooling, the outlet temperature and heat exchange rate are reduced in the early stage owing to the longer cooling period before crystallization is triggered. However, once crystallization occurs, the heat exchange rate increases suddenly. In Fig. 18, the case with 2 °C supercooling is used as the benchmark, and the relative difference in the total output energy (RDE) of each case is depicted. The RDE can be obtained using Eq. (33). Before crystallization occurred, the total output energy decreased as the supercooling deepened. However, the faster crystallization process caused the accumulated heat output of the serious supercooling case to be higher than that of the slight supercooling case following crystallization.

$$RDE(t) = \frac{Q_{out}(t) - Q_{out}(t,sup=2)}{Q_{out}(t,sup=2)}, \tag{33}$$

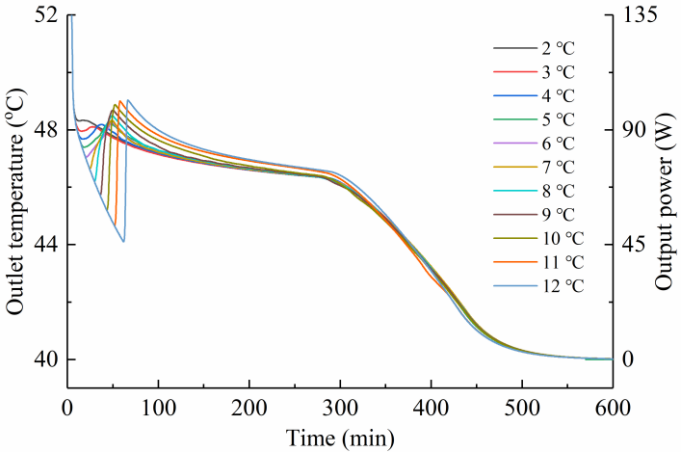

Fig. 17. Outlet temperature evolution during supercooling with different supercooling degree

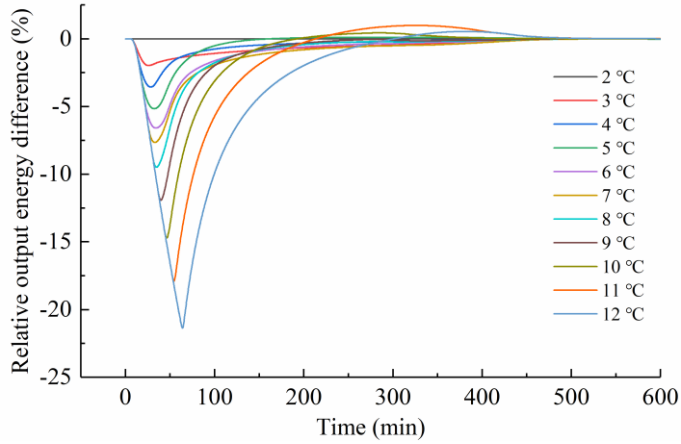

Fig. 18. Relative difference in total output energy during supercooling with different supercooling degree

4.2 Influence of initial temperature and inlet temperature

Figure. 19 shows the change in the outlet temperature under different supercooling conditions when the initial temperature was 60 °C and the inlet temperatures were 20, 30, and 40 °C. When the inlet temperature increased, the temperature difference and heat exchange between the HTF and PCM decreased, and thus, the time for triggering crystallization was delayed. Deeper supercooling resulted in a longer delay. Furthermore, the

outlet temperature change caused by the crystallization gradually increased. When the supercooling degree was 12 °C, the increase in outlet temperature with inlet temperatures of 20, 30, and 40 °C was 3.31, 4.10, and 4.87 °C, respectively. Fig. 20 depicts the outlet temperature when the inlet temperature was 40 °C and the initial temperatures were 60, 70, and 80 °C. The increase in the initial temperature also delayed the triggering of the crystallization. Furthermore, the minimum temperature was increased before the temperature increase, and the maximum temperature was reduced thereafter. In general, the increase in the initial temperature and decrease in the inlet temperature (the increased temperature difference between the HTF and PCM) weakened the outlet temperature fluctuations due to the crystallization, and the influence of the inlet temperature became more prominent.

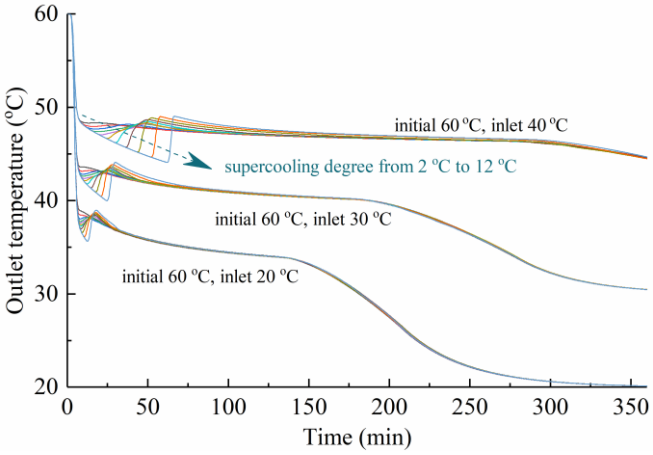

Fig. 19. Outlet temperature under different inlet temperatures and supercooling degree

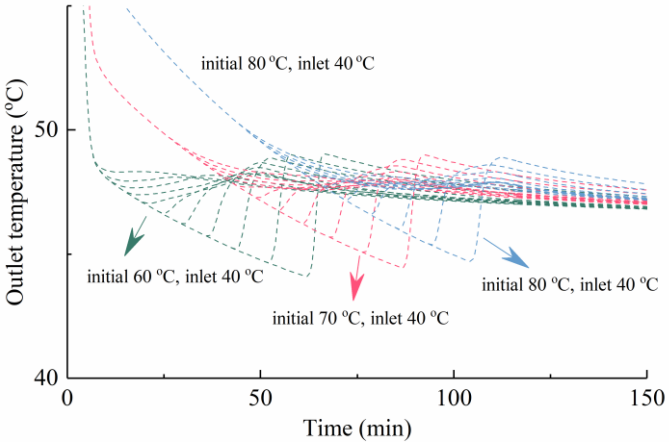

Fig. 20. Outlet temperature under different initial temperatures and supercooling degree

4.3 Comparison of models

The complete model was compared with the single-growth model described in section 3.2, the model with instantaneous crystallization (the no-growth model), and the model that neglects supercooling (no-supercooling model). The initial temperature was 60 °C, the inlet temperature was 40 °C, and the supercooling degree was 7 °C. Fig. 21 shows the temperature field changes of the four models; the bottom cells represent the HTF zone. All the models that considered supercooling released sensible heat to the HTF before crystallization was triggered, and their temperature fields were exactly the same (time = 10 min in Fig. 21a, b, and c). In the no-supercooling model, latent heat was released directly after the temperature entered the phase-change interval. Therefore, the temperature field was relatively uniform (time = 10 min in Fig. 21d). Once the crystallization was triggered, solidification started from the trigger point in the complete and single-growth models, and the

temperature near that point gradually increased. The temperature field difference between them was small, as indicated by time = 30 min in Fig. 21a and b. In the no-growth model, the crystallization was completed instantly, and the temperature field became similar to that of the no-supercooling model (Fig. 21c and d). At 120 min, certain zones had completely released their latent heat, and their temperatures were significantly lower than the others.

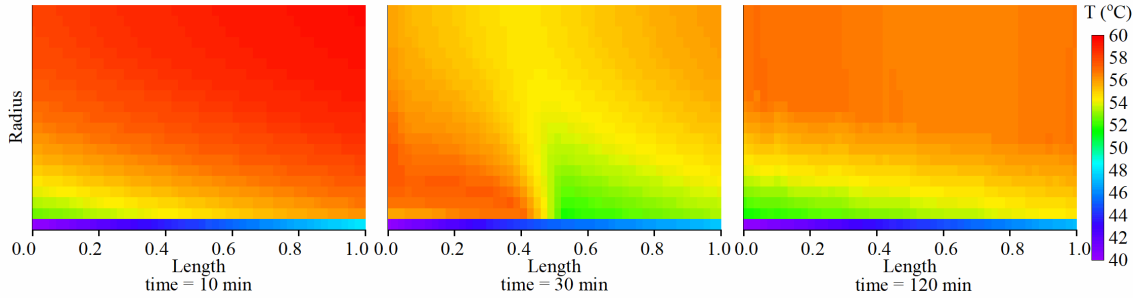

a. Complete model

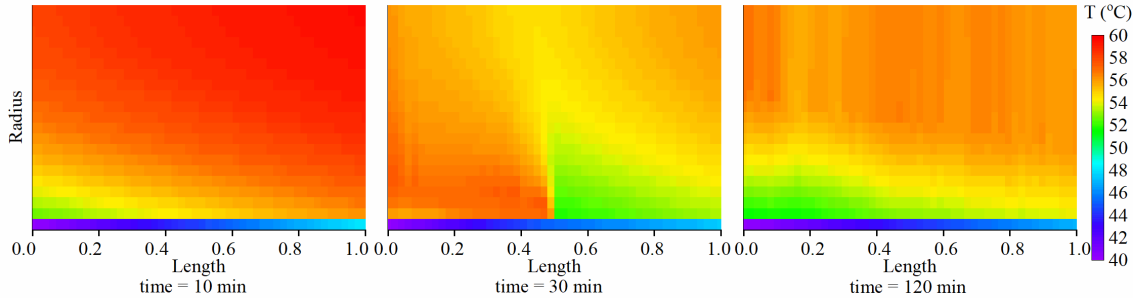

b. Single-growth model

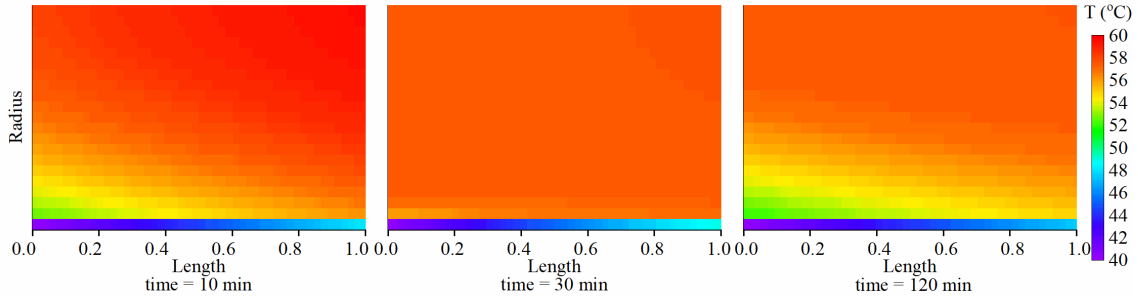

c. No-growth model

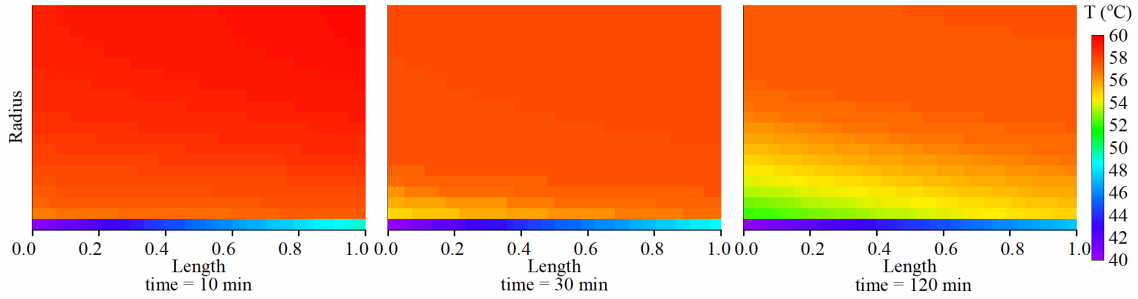

d. No-supercooling model

Fig. 21. Temperature field changes of four models

Fig. 22 shows the temperature changes of three points inside the PCM zone: point a (400 mm, 25.1 mm), point b (400 mm, 33.8 mm), and point c (400 mm, 42.4 mm). The curves of 0 to 60 min are enlarged to observe the crystallization process more clearly. When the temperature decreased to the phase-change interval, the no-

supercooling model performed distinctly from the others. Once the crystallization was triggered, the overall PCM temperature of the no-growth model increased to the highest point instantaneously. In the complete and single-growth models, each point started to heat up after the crystallization front was reached, and the latter had a higher heating rate. Because each point started to solidify at a different temperature, their crystallization speed and time taken to reach the highest temperature also differed.

Fig. 23 presents the outlet temperature and total output energy of the four models. Because the initial temperatures were the same, the total energies that could be output were also the same. The no-growth and no-supercooling models output heat more rapidly. The main differences among the models appeared in the output temperature during the crystallization process: the maximum deviations between the complete and single-growth models, complete and no-growth models, and complete and no-supercooling models were 0.4, 2.1, and 2.0 °C, respectively, and the corresponding deviations of the heat transfer power were 2.8%, 30.9%, and 30.5%, respectively.

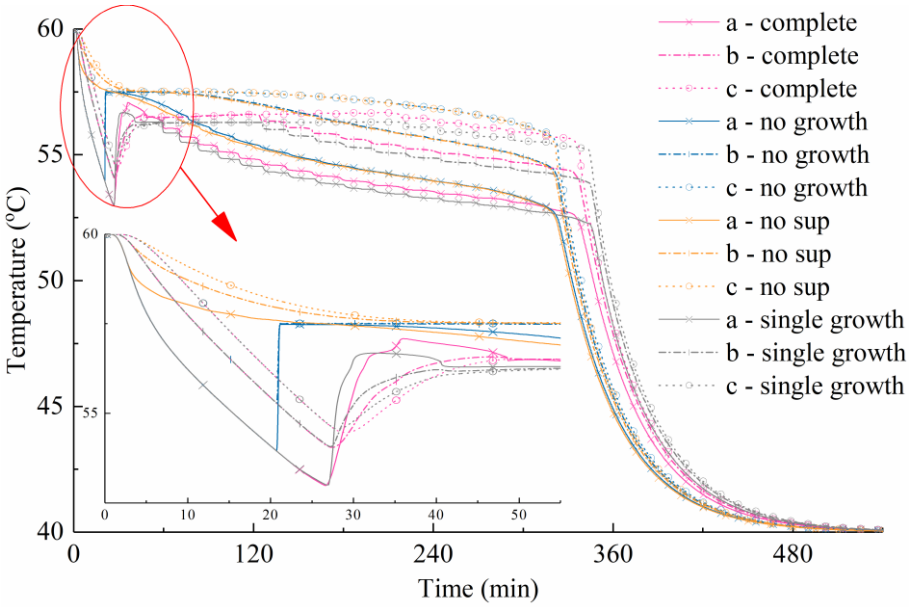

Fig. 22. Temperature changes at the monitoring points obtained with four models

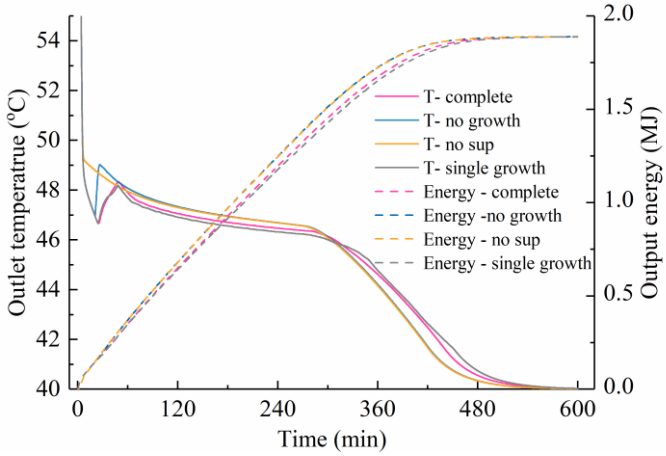

Fig. 23. Comparison of the outlet temperatures and total output energies of four models

The differences among the four models were statistically analyzed with supercooling degrees ranging from 2 to 12 °C under the same boundary conditions. Fig. 24 shows the difference of the output power between the no-growth and complete models. Two peaks in the curves can be observed. The first was due to the different durations of the crystallization process. As this also caused the PCM to have different remaining energies, the second peak appeared later. It can be seen from Fig. 25 that the relative difference between their output power

in the crystallization period reached 89% at the maximum and -39% in the later stage of the heat release. From another perspective, considering the crystallization to be instantaneous caused a part of the heat to be released earlier (from the second peak to the first peak). As the supercooling deepened, the value of the first peak increased. Meanwhile, its area decreased, which implies that the energy that was released in advance decreased. Moreover, the difference between the two models decreased. This is because the crystallization speed and the solidification speed increased (as described in Fig. 17), which reduced the gap between the two models. The ratio of the energy that was released in advance to the total output energy was used to indicate the difference between the two models, and the results are depicted in Fig. 26.

Similarly, the gaps between the no-supercooling and complete models are shown in Figs. 27, 28 and 29. Because it ignored supercooling, the no-supercooling model maintained a higher temperature and output power during the early stage, and the heat that should have been released following crystallization was released in advance, which introduced a large difference. From Fig. 28, it can be seen that this difference increased significantly as the supercooling deepened. In addition, as shown in Fig. 29, the maximum relative difference of their output power is 93% in the crystallization trigger period and -41% in the late stage of the heat release.

Figs. 30 to 32 show the differences between the single-growth and complete models. The addition of the solidification speed (*vs*) affected the change rate of the temperature field and the starting temperature for each node to crystallize, which influenced the crystallization speed (*v*). As can be seen from Fig. 31, the output powers of the two models have a huge relative deviation, especially in the later stage of heat release in which the gap reached 90%. The mutual influence between the two speeds caused the difference to exhibit no apparent regularity with the supercooling change. In general, the single-growth model overestimated the heat release rate in the early and late stages, while underestimating the mid-term heat release rate.

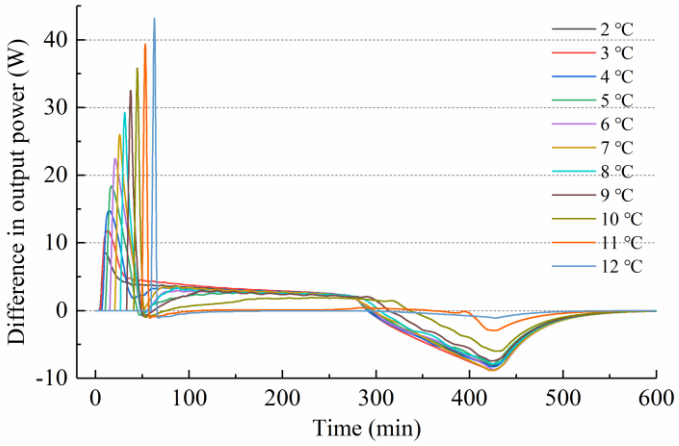

Fig. 24. Difference in output power between no-growth and complete models

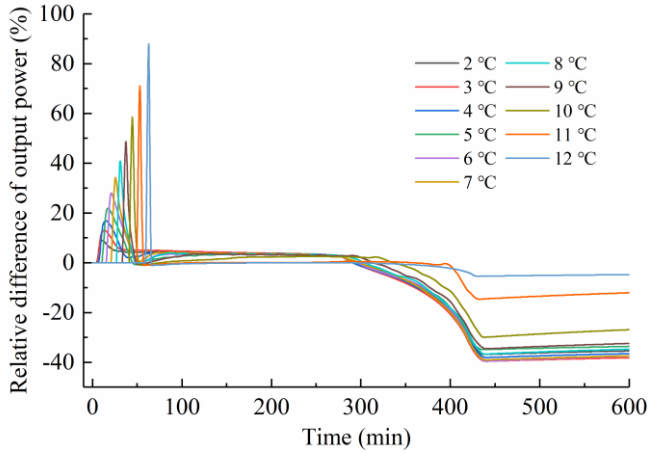

Fig. 25. Relative difference in output power between no-growth and complete models

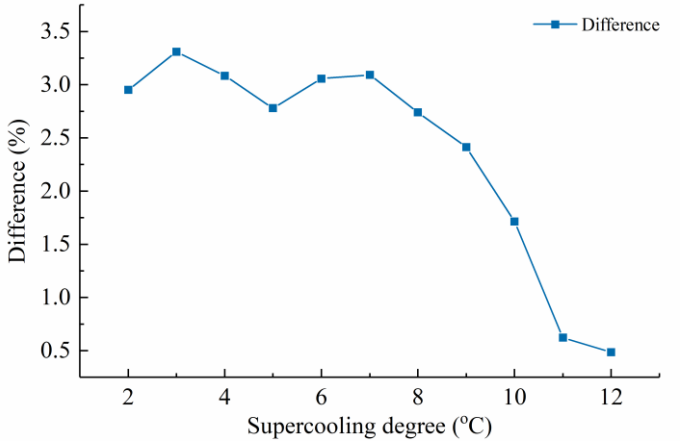

Fig. 26. Proportion of heat released in advance in no-growth model

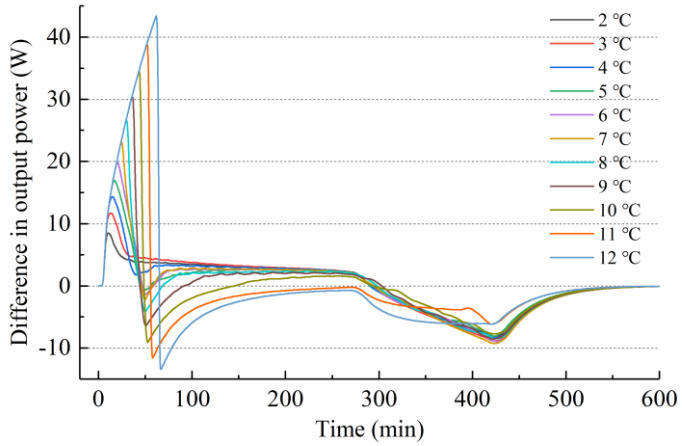

Fig. 27. Difference in output power between no-supercooling and complete models

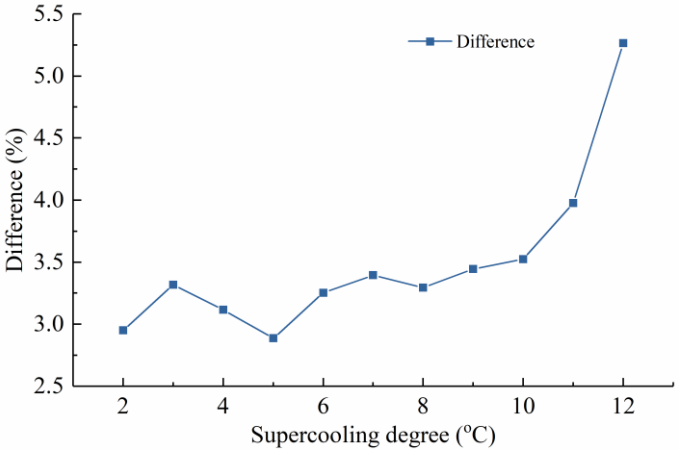

Fig. 28. Proportion of heat released in advance in no-supercooling model

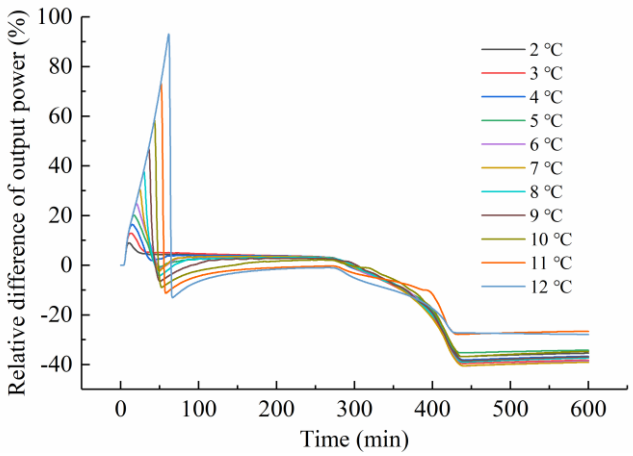

Fig. 29. Relative difference in output power between no-supercooling and complete models

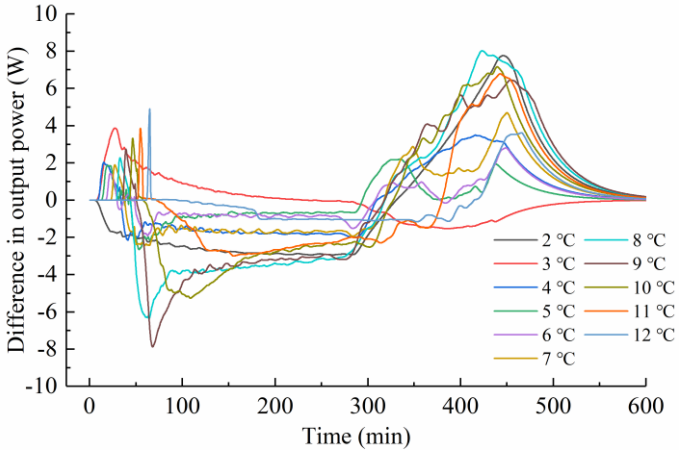

Fig. 30. Difference in output power between single-growth and complete models

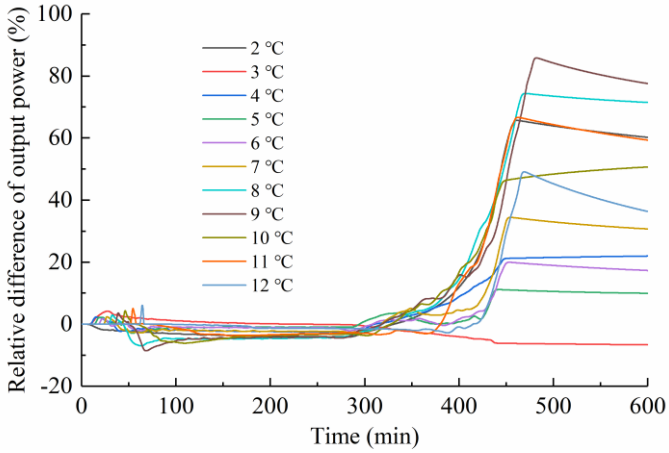

Fig. 31. Relative difference in output power between single-growth and complete models

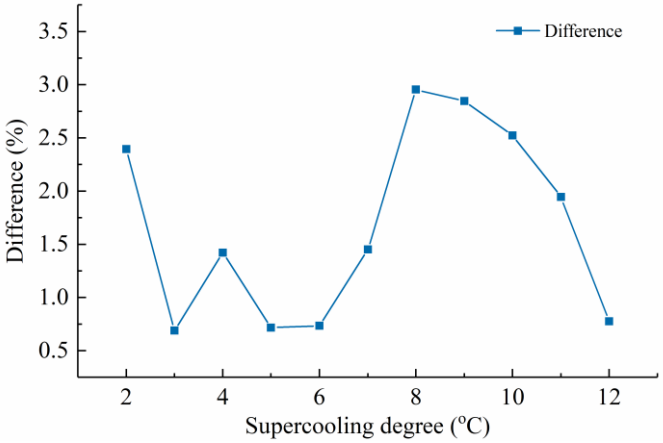

Fig. 32. Proportion of heat released in advance in single-growth model

The heat in the PCM may not be completely released in practical applications. The output energy is dependent on factors such as the initial temperature, inlet temperature, and heat release duration. Therefore, the differences in the models may be larger than those in the previous analysis with a shorter heat release time. To consider this factor, the proportion of heat that was released in advance to the accumulated heat that was released in each time step was determined, and the maximum value was selected to represent the relative difference between the models, as indicated in Eq. (34). This method was used to obtain the maximum difference between the complete model and the other three models in 99 cases (396 simulations) under different boundary conditions. As illustrated in Fig. 33, the relative gap between the no-growth and complete models was reduced significantly with an increase in the initial temperature and a decrease in the inlet temperature. Intuitively, as the supercooling deepened, the two models treated the crystallization process more similarly and their temperature field difference decreased. However, when the supercooling was low, the temperature change during the crystallization process was small, and there was no significant difference between the temperature fields of the two models. Thus, as the supercooling deepened, the relative gap between the two models first increased and then decreased, reaching a maximum when the supercooling degree was approximately 6 °C. The maximum value for all cases was approximately 9%. The decrease in the inlet temperature and increase in the initial temperature also caused the relative gap between the no-supercooling and complete models to decrease, as illustrated in Fig. 34. As the supercooling deepened, its influence on the temperature field increased, and the gap increased significantly. When the supercooling degree was 12 °C, the maximum relative difference reached 33%. From Fig. 35, it can be seen that the gap between the single-growth and complete models exhibited no obvious change, and the maximum relative difference was 3%.

$$\text{Relative difference} = \max\left[\frac{Qout_i(t) - Qout_{com}(t)}{Qout_{com}(t)}\right], \tag{34}$$

where $Qout_i$ is the output energy for a model (no-growth, single-growth, and no-supercooling models).

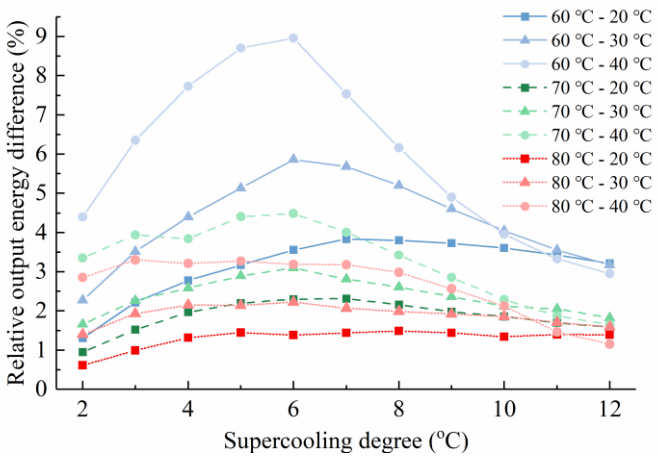

Fig. 33. Relative difference between no-growth and complete models under different cases

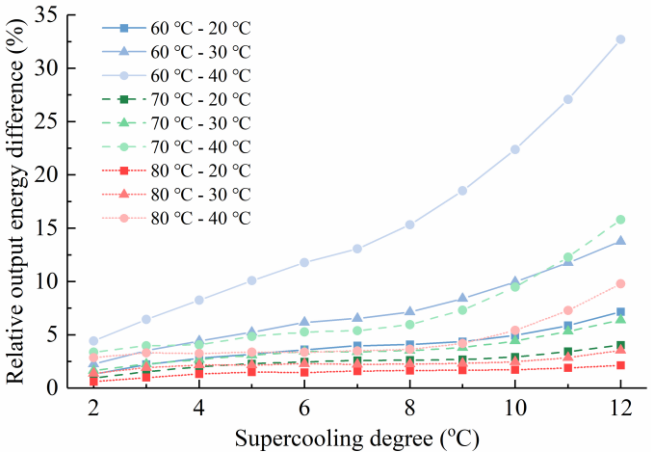

Fig. 34. Relative difference between no-supercooling and complete models under different cases

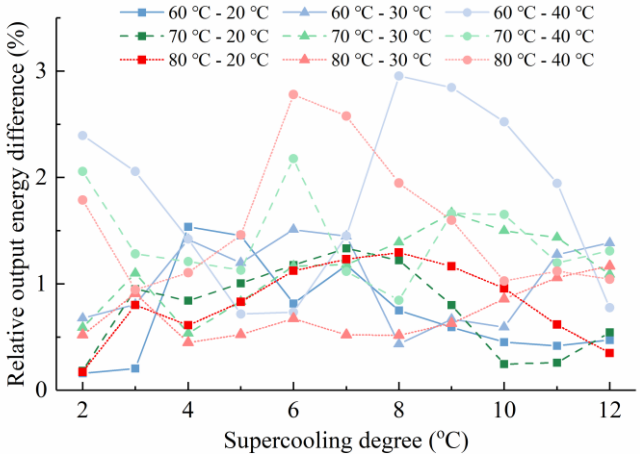

Fig. 35. Relative difference between single-growth and complete models under different cases

5. Conclusions

A two-dimensional PCM heat transfer model was constructed using the implicit finite difference method, which focuses on the supercooling and phase-change hysteresis in the cooling process. This model uses the crystallization speed to control the crystallization start time of each cell, the solidification speed to control the heating process, and the cellular automata method to determine the growth direction of the crystal. A concentric tube exchanger system was built using a SAT/EG composite PCM. The accuracy of the numerical model in

simulating melting, cooling, and triggering of crystallization in a stable supercooled state, as well as triggering of crystallization during cooling, were verified experimentally based on the temperature field changes. The effects of the supercooling, initial temperature, and inlet temperature on the heat transfer rate were investigated. Supercooling was found to delay the crystallization triggering time and reduce the heat transfer rate. However, serious supercooling accelerates the crystallization process and results in the PCM reaching a higher stable temperature. Therefore, the accumulative output energy was greater than that in the slight supercooling case at certain moments. The increase in the initial temperature and decrease in the inlet temperature reduced the sharp increase in outlet temperature caused the crystallization process, and the effect of the decrease in the inlet temperature was greater. This numerical model (complete model) was compared with the no-growth, no-supercooling, and single-growth models. It was demonstrated that there is a huge relative difference between the output powers of the other three models and the complete model. In addition, ignoring the crystal growth process causes a part of the heat in the PCM to be released in advance. This part of the heat can reach up to 9% of the released heat under different parameters, and ignoring supercooling intensifies this phenomenon. When the supercooling degree was 12 °C, this proportion was as high as 33%, and it increased further as the supercooling deepened. The single-growth model caused a part of the heat to be released early and a part of the heat to be released later, resulting in a maximum relative difference of 3%.

Acknowledgement

The authors acknowledge the support from the Chongqing (China) Science & Technology Commission (Project No. cstc2018jcyjAX0072).

Appendix

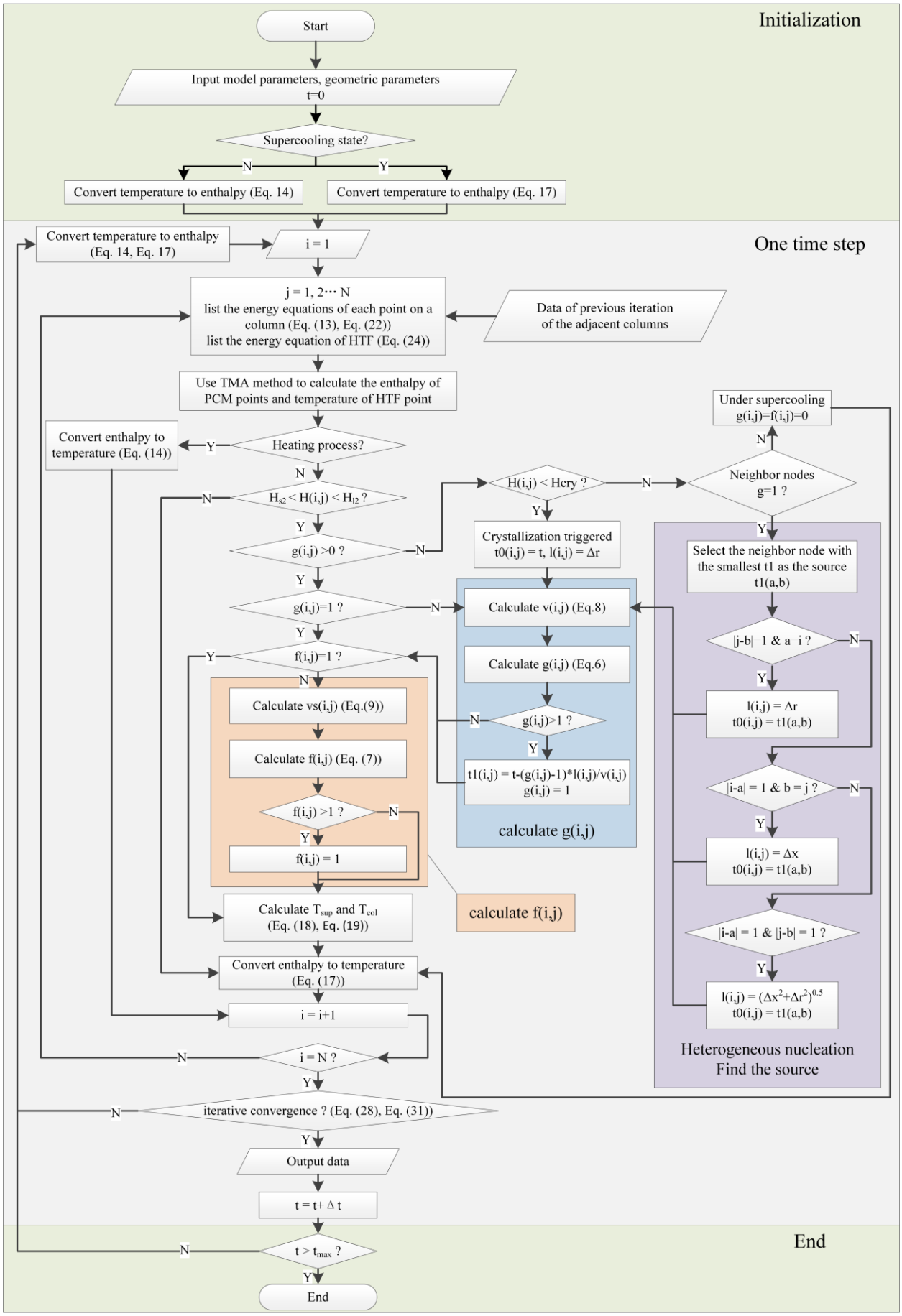

Fig. 1. Operation logic of the program

References

[1] Yu K, Liu Y, Yang Y. Review on form-stable inorganic hydrated salt phase change materials: Preparation, characterization and effect on the thermophysical properties. Appl Energy. 2021;292:116845. https://doi.org/10.1016/j.apenergy.2021.116845

[2] Yan TS, Li TX, Xu JX, Chao JW. Understanding the transition process of phase change and dehydration reaction of salt hydrate for thermal energy storage. Appl Therm Eng. 2020;166:114655. https://doi.org/10.1016/j.applthermaleng.2019.114655

[3] Lin J, Zhao Q, Huang H, Mao H, Liu Y, Xiao Y. Applications of low-temperature thermochemical energy storage systems for salt hydrates based on material classification: A review. Sol Energy. 2021;214:149-78. https://doi.org/10.1016/j.solener.2020.11.055

[4] Mehrali M, ten Elshof JE, Shahi M, Mahmoudi A. Simultaneous solar-thermal energy harvesting and storage via shape stabilized salt hydrate phase change material. Chem Eng J. 2021;405:126624. https://doi.org/10.1016/j.cej.2020.126624

[5] Kumar N, Hirschey J, LaClair TJ, Gluesenkamp KR, Graham S. Review of stability and thermal conductivity enhancements for salt hydrates. J Energy Storage. 2019;24:100794. https://doi.org/10.1016/j.est.2019.100794

[6] Lin Y, Alva G, Fang G. Review on thermal performances and applications of thermal energy storage systems with inorganic phase change materials. Energy. 2018;165:685-708. https://doi.org/10.1016/j.energy.2018.09.128

[7] Furbo S, Fan J. Heat storage based on a NaCH3COO water mixture for solar heating systems. technical report SR-12-10, Department of Civil Engineering, Technical University of Denmark; 2012.

[8] Safari A, Saidur R, Sulaiman FA, Xu Y, Dong J. A review on supercooling of Phase Change Materials in thermal energy storage systems. Renew Sustain Energy Rev. 2017;70:905-19. https://doi.org/10.1016/j.rser.2016.11.272

[9] Barz T, Sommer A. Modeling hysteresis in the phase transition of industrial-grade solid/liquid PCM for thermal energy storages. Int J Heat Mass Transf. 2018;127:701-13. https://doi.org/10.1016/j.ijheatmasstransfer.2018.08.032

[10] Jin X, Hu H, Shi X, Zhang X. Energy asymmetry in melting and solidifying processes of PCM. Energy Convers Manag. 2015;106:608-14. https://doi.org/10.1016/j.enconman.2015.10.001

[11] Jin X, Hu H, Shi X, Zhou X, Yang L, Yin Y, et al. A new heat transfer model of phase change material based on energy asymmetry. Appl Energy. 2018;212:1409-16. https://doi.org/10.1016/j.apenergy.2017.12.103

[12] Tabares-Velasco PC, Christensen C, Bianchi M. Verification and validation of EnergyPlus phase change material model for opaque wall assemblies. Build Environ. 2012;54:186-96. https://doi.org/10.1016/j.buildenv.2012.02.019

[13] Biswas K, Shukla Y, Desjarlais A, Rawal R. Thermal characterization of full-scale PCM products and numerical simulations, including hysteresis, to evaluate energy impacts in an envelope application. Appl Therm Eng. 2018;138:501-12. https://doi.org/10.1016/j.applthermaleng.2018.04.090

[14] Ivshin Y, Pence TJ. A constitutive model for hysteretic phase transition behavior. Int J Eng Sci. 1994;32:681-704. https://doi.org/10.1016/0020-7225(94)90027-2

[15] Goia F, Chaudhary G, Fantucci S. Modelling and experimental validation of an algorithm for simulation of hysteresis effects in phase change materials for building components. Energy Build. 2018;174:54-67. https://doi.org/10.1016/j.enbuild.2018.06.001

[16] Kousksou T, El Rhafiki T, Mahdaoui M, Bruel P, Zeraouli Y. Crystallization of supercooled PCMs inside emulsions: DSC applications. Sol Energy Mater Sol Cells. 2012;107:28-36. https://doi.org/10.1016/j.solmat.2012.07.023

[17] Bony J, Citherlet S. Numerical model and experimental validation of heat storage with phase change materials. Energy Build. 2007;39:1065-72. https://doi.org/10.1016/j.enbuild.2006.10.017

[18] Delcroix B, Kummert M, Daoud AJJoBPS. Development and numerical validation of a new model for walls with

phase change materials implemented in TRNSYS. J Build Perform Simul. 2017;10:422-37. https://doi.org/10.1080/19401493.2017.1280087
[19] Beaupere N, Soupremanien U, Zalewski L. Experimental measurements of the residual solidification duration of a supercooled sodium acetate trihydrate. Int J Therm Sci. 2020;158:106544. https://doi.org/10.1016/j.ijthermalsci.2020.106544
[20] Günther E, Mehling H, Hiebler S. Modeling of subcooling and solidification of phase change materials. Model Simul Mater Sci Eng. 2007;15:879-92. https://doi.org/10.1088/0965-0393/15/8/005
[21] Zhou G, Han Y. Numerical simulation on thermal characteristics of supercooled salt hydrate PCM for energy storage: Multiphase model. Appl Therm Eng. 2017;125:145-52. https://doi.org/10.1016/j.applthermaleng.2017.07.010
[22] Uzan AY, Kozak Y, Korin Y, Harary I, Mehling H, Ziskind G. A novel multi-dimensional model for solidification process with supercooling. Int J Heat Mass Transf. 2017;106:91-102. https://doi.org/10.1016/j.ijheatmasstransfer.2016.10.046
[23] Ma Z, Bao H, Roskilly AP. Study on solidification process of sodium acetate trihydrate for seasonal solar thermal energy storage. Sol Energy Mater Sol Cells. 2017;172:99-107. https://doi.org/10.1016/j.solmat.2017.07.024
[24] Munakata T, Nagata SJNKGRBHtotJSoMEPB. Study on Solidification Process of Sodium Acetate Trihydrate from Supercooled State. Trans JSME. 2008;74:2365-71. https://doi.org/10.1299/kikaib.74.2365
[25] Dietz PL, Brukner JS, Hollingsworth CA. Linear Crystallization Velocities of Sodium Acetate in Supersaturated Solutions. J Phys Chem. 1957;61:944-8. https://doi.org/10.1021/j150553a023
[26] Huang H, Zhang Y, Wu H, Lin J, Zhao Q, Zhou T, et al. Crystallization speed and solidification time of sodium acetate trihydrate–graphite composite phase change materials during solidification. J Energy Storage. 2021;40:102820. https://doi.org/10.1016/j.est.2021.102820
[27] Al-Saadi SN, Zhai Z. Modeling phase change materials embedded in building enclosure: A review. Renew Sustain Energy Rev. 2013;21:659-73. https://doi.org/10.1016/j.rser.2013.01.024
[28] Zhou T, Xiao Y, Liu Y, Lin J, Huang H. Research on cooling performance of phase change material-filled earth-air heat exchanger. Energy Convers Manag. 2018;177:210-23. https://doi.org/10.1016/j.enconman.2018.09.047
[29] El Rhafiki T, Kousksou T, Jamil A, Jegadheeswaran S, Pohekar SD, Zeraouli Y. Crystallization of PCMs inside an emulsion: Supercooling phenomenon. Sol Energy Mater Sol Cells. 2011;95:2588-97. https://doi.org/10.1016/j.solmat.2011.03.027
[30] Beaupere N, Soupremanien U, Zalewski L. Nucleation triggering methods in supercooled phase change materials (PCM), a review. Thermochim Acta. 2018;670:184-201. https://doi.org/10.1016/j.tca.2018.10.009
[31] Neumann J, Burks AW. Theory of self-reproducing automata: University of Illinois press Urbana; 1966.
[32] Dannemand M, Schultz JM, Johansen JB, Furbo S. Long term thermal energy storage with stable supercooled sodium acetate trihydrate. Appl Therm Eng. 2015;91:671-8. https://doi.org/10.1016/j.applthermaleng.2015.08.055